journal of the mechanical behavior of biomedical materials 144 (2023) 105989

Contents lists available at ScienceDirect

Journal of the Mechanical Behavior of Biomedical Materials

journal homepage: www.elsevier.com/locate/jmbbm

Improved biomechanical behavior of 316L graded scaffolds for bone tissue regeneration produced by laser powder bed fusion

Maria Laura Gatto [a,1,*], Giorgia Cerqueni [b,1], Riccardo Groppo [c], Eleonora Santecchia [a], Emanuele Tognoli [d], Silvio Defanti [d], Monica Mattioli-Belmonte [b], Paolo Mengucci [e]

[a] Department DIISM, Università Politecnica Delle Marche, Via Brecce Bianche 12, 60131, Ancona, Italy
[b] Department DISCLIMO & UdR INSTM, Università Politecnica Delle Marche, Via Tronto 10/a, Ancona, 60126, Italy
[c] 3D4MEC S.r.l, Via Porrettana 48, 40037, Sasso Marconi, BO, Italy
[d] Department of Engineering "Enzo Ferrari", Università di Modena e Reggio Emilia, Via Vivarelli 10, 41125, Modena, Italy
[e] Department SIMAU & UdR INSTM, Università Politecnica Delle Marche, Via Brecce Bianche 12, 60131, Ancona, Italy

ARTICLE INFO

Keywords:
Bone tissue
Graded lattice scaffold
316L stainless steel
Laser powder bed fusion
Biomechanical performance
MG-63 adhesion

ABSTRACT

Graded lattice scaffolds based on rhombic dodecahedral (RD) elementary unit cell geometry were manufactured in 316L stainless steel (SS) by laser powder bed fusion (LPBF). Two different strategies based on varying strut thickness layer-by-layer in the building direction were adopted to obtain the graded scaffolds: a) decreasing strut size from core to edge to produce the dense-in (DI) structure and b) increasing strut size in the same direction to produce the dense-out (DO) structure. Both graded structures (DI and DO) were constructed with specular symmetry with respect to the central horizontal axis. Structural, mechanical, and biological characterizations were carried out to evaluate feasibility of designing appropriate biomechanical performances of graded scaffolds in the perspective of bone tissue regeneration. Results showed that mechanical behavior is governed by graded geometry, while printing parameters influence structural properties of the material such as density, textures, and crystallographic phases. The predominant failure mechanism in graded structures initiates in correspondence of thinner struts, due to high stress concentrations on strut junctions. Biological tests evidenced better proliferation of cells in the DO graded scaffold, which in turn exhibits mechanical properties close to cortical bone. The combined control of grading strategy, printing parameters and elementary unit cell geometry can enable implementing scaffolds with improved biomechanical performances for bone tissue regeneration.

1. Introduction

Among the various metals used for bone tissue regeneration, the most cost-effective solution for short-term implants is 316L stainless steel (316L SS) (Luo et al., 2018). 316L SS is widely used in the bone repair or replacement for acetabular cup of hip joint, plates and screws and oral grafts (Bai et al., 2019; Majumdar et al., 2018), due to the bone-adequate mechanical properties, acceptable biocompatibility, high corrosion resistance and low cost (Lodhi et al., 2019; Fellah et al., 2013). Nevertheless, prolonged contact with chloride ions in the physiological environment causes corrosion of surface passive film, with the release of iron ions and consequent inflammatory risk (Peng et al., 2019).

In this case, appropriate choice of the production technology, which determines the corrosion behavior of the material, can be used to reduce potential implant failure. Al-Mamun et al. (2020) reported on the superior biocompatibility in aggressive biological environments of the additively manufactured 316L SS as compared to the wrought alloy. In particular, they showed that the high corrosion resistance of samples produced by laser powder bed fusion (LPBF) limited the release of toxic ions into the biological environment, resulting in better viability and proliferation of pre-osteoblast cells (Al-Mamun et al., 2020). Furthermore, Kong et al. (2018) found an increase in cell concentration and proliferation with laser power so much that, at around 200 W, samples showed considerably greater biocompatibility than quenched 316L SS.

In addition to biocompatibility, an ideal scaffold for bone regeneration should possess high porosity with interconnected and well-distributed pore network. Effect of porosity, pore size and pore

* Corresponding author.
E-mail address: m.l.gatto@univpm.it (M.L. Gatto).
[1] Maria Laura Gatto and Giorgia Cerqueni equally contributed to the paper.

https://doi.org/10.1016/j.jmbbm.2023.105989
Received 1 July 2022; Received in revised form 20 June 2023; Accepted 22 June 2023
Available online 23 June 2023

interconnectivity are encompassed in scaffold permeability performance. Permeability refers to scaffold ability of mass transport throughout the 3D structure (Dias et al., 2012). Transport of oxygen, nutrients and metabolic waste are necessary for short-term cell recruitment and penetration, and long-term vascularization.

Moreover, scaffold mechanical properties are required to match with implant tissue to prevent stress shielding effects (bone loosening) and to avoid mechanical failure under the anatomical load (Wang et al., 2016).

Mechanical performance and biological response of a device can be set tailoring geometry. Periodic arrangement of elementary unit cells in the 3D space (lattice) allows customizing pore size and shape as well as porosity, which affect the mechanical properties of the scaffold. In addition, an interconnected pore network promotes cell migration by enabling nutrients and oxygen apport to cells (Onal et al., 2018). However, blood capillaries formation and consequent tissue vascularization need open high-porous structure, with the risk to mismatch with the required mechanical properties (Onal et al., 2018).

Although lattice structures result quite distant from bone morphology (Bai et al., 2019), in biomedical applications lattice structures can be used to reduce the stiffness of metallic medical implants to be closer to that of bone, thereby avoiding stress shielding while allowing fluid flow due to their porosity with a large surface area-to-volume ratio, to facilitate osseointegration (Maconachie et al., 2019).

Strut-based lattice structures are often chosen for their simplicity of design, but strut-based topologies have also been generated from topological optimization to maximize the efficiency of material distribution within the lattice structure (Xiao et al., 2018a; Xu et al., 2016). Alternative topologies to strut-based structures are lattice structures with unit cells based on triply periodic minimal surfaces (TPMS) such as the Schoen gyroid, Schwartz diamond and Neovius (Maconachie et al., 2019). TPMS lattice structures have potential advantages over strut-based topologies in terms of manufacturability and bone fixation (Wang et al., 2021).

Based on a finite element analysis, Ali et al. (Ali and Sen, 2017) concluded that at the same porosity, strut-based scaffolds exhibited elastic field behavior and compressive strength better mimicking properties of cancellous bone than gyroid scaffolds. Furthermore, higher permeability of strut-lattice promotes better cell biological activities than gyroid structure.

Graded lattice structure is a potential solution to meet both mechanical and long-term biological needs for bone regeneration, providing adaptative porous gradient and better miming natural bone (Al-Ketan et al., 2020). Functional grading (variation of size, typology, material, or strut diameter) (Bai et al., 2019; Li et al., 2016; Ren et al., 2022; Caiazzo et al., 2022) also allows programming deformation behavior of the scaffold, by controlling the local relative density of unit cells. Thus, graded reticular structures enable to design body implants with local stiffness matching the stiffness of the target bone (Al-Ketan, 2021). The mechanical behavior of graded structures compared to the uniform geometry have been reported in literature mainly for Ti6Al4V (Onal et al., 2018; Li et al., 2016) and more recently for a 17-4-PH stainless steel (Caiazzo et al., 2022). All these papers showed a global mechanical behavior of uniform structures characterized of oscillations in the stress-strain curves typical of the layer-by-layer collapse. On the contrary, the graded structures generally showed stress-strain curves without oscillations.

Additive Manufacturing (AM) is a suitable technology to produce graded lattice structures. In particular, laser powder bed fusion (LPBF) allows to achieve high accuracy of internal architecture, also in case of intricate pattern and micro-scaled reticula (du Plessis et al., 2021; Zhong et al., 2019).

Literature data on 316L SS LPBF lattice scaffolds for bone implants evidence a relation between mechanical properties and porosity, due to unit cell topology, but there is lack of experiments on graded lattice scaffolds, designed to guide biomechanical response for bone tissue regeneration.

To the best of authors' knowledge, until now studies on 316L SS scaffolds produced by LPBF technology were limited to gyroid, lattice and topology-optimized lattice geometries (Zhong et al., 2019; Čapek et al., 2016; Fousová et al., 2017; Xiao et al., 2018b; Cao et al., 2018). The only study on optimization of a 316L SS LPBF graded lattice scaffold, for programming its plastic deformation behavior, is not applied to biomedical implants (Al-Ketan, 2021).

Aim of this work is to fill the gap, focusing on the biomechanical performances of graded strut-based scaffolds in 316L SS, aiming also to demonstrate that properly designing the graded structures allows obtaining scaffolds with biomechanical performances suitable for bone tissue regeneration. As a first approach, a very simple structure with unidirectional grading along the build direction was manufactured by the LPBF technology in 316L SS.

Graded geometries based on rhombic dodecahedron (RD) elementary unit cell were designed by linearly varying strut diameter across layers along the build direction. The RD elementary unit cell was adopted based on the paper by Li et al. (2016), while the graded lattice was obtained by gradually changing the strut size as proposed by Onal et al. (2018).

Two different scaffold patterns were built by changing strut size in decremental (dense-in) and incremental (dense-out) values from core to edges, while mirroring the structure on the central horizontal axis. Considering that the mechanical response of uniform structures reported in the literature (Onal et al., 2018; Li et al., 2016; Ren et al., 2022; Caiazzo et al., 2022) showed a similar behavior without oscillations in the stress-strain curve, this study focused the attention exclusively on the mechanical behavior of graded structures. After production, the scaffolds did not undergo any post-processing surface treatment, to investigate their mechanical and biological performances in the as-produced state.

The mechanical performances of scaffolds were experimentally investigated, and results were related to their micro- and macro-structure. Mechanical behavior of dense-in (DI) and dense-out (DO) graded lattice scaffolds were compared to lattice and optimized-lattice geometries from literature, as well as to bone tissue, in the perspective of bone implant. In this work, the scaffold with the DO graded geometry showed mechanical properties close to cortical bone. Biological tests also allowed investigating influence of scaffold geometry on evolution of cells colonization. Results evidenced that graded lattice geometry can be used to design both mechanical and biological behavior of 316L scaffolds for bone tissue applications.

2. Materials and methods

2.1. Scaffold design

Dense-in (DI) and dense-out (DO) graded lattice scaffold geometries (Fig. 1) were designed by Autodesk Netfabb (Inc., San Rafael, CA). Cubic scaffolds 10 mm side, total scaffold volume $V_s = 1000\ mm^3$, were obtained by repeating in space rhombic dodecahedral (RD) elementary unit cell (Fig. 1a). The graded structure was achieved by varying strut size of elementary unit cell layer by layer along the building direction (unidirectional). In this way, scaffold porosity inversely varied with strut thickness (ST). Values of ST in the range 0.25–0.75 mm, with step size 0.25 mm, were used. In DI geometry strut size decreased from core to edge (Fig. 1b), while in DO geometry strut size increased from core to edge (Fig. 1c). Both geometries were built in specular symmetry from central horizontal axis, thus scaffold was composed of total five layers (Fig. 1b and c).

Values from STL files of total volume of material (V_{mSTL}), fractional density (ρ_{STL}) and specific surface (A_{sSTL}) of DI and DO geometries are reported in Table 1.

The specific surface A_s (unit: mm^{-1}) is defined as:

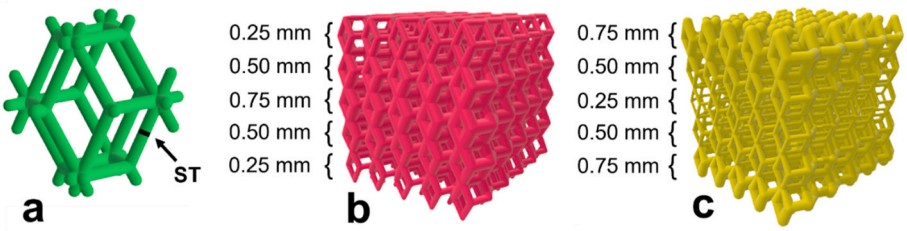

Fig. 1. Schematics of rhombic dodecahedral geometry: a) elementary unit cell, b) dense-in (DI) graded lattice geometry, c) dense-out (DO) graded lattice geometry. Strut thickness (ST) in a) evidenced by arrow. Values of ST (unit: mm) for DI and DO layers are reported next to lattices.

Table 1
Total material volume (V_{mSTL}), fractional density (ρ_{STL}) and specific surface (A_{sSTL}) values from STL file for DO and DI geometries.

Geometry	V_{mSTL} (mm^3)	ρ_{STL} (%)	A_{sSTL} (mm^{-1})
Dense-in (DI)	425	42	5
Dense-out (DO)	276	28	7

$$A_s = \frac{S_m}{V_m} \tag{1}$$

where S_m is the total surface of the material and V_m the material volume.

2.2. Scaffold production

Scaffolds were produced starting from raw powder of 316L stainless steel (SS) from LPV CARPENTER Technology, by using laser powder bed fusion (LPBF) technology in *3D4steel* manufacturing system (3D4Mec Srl, Sasso Marconi, Italy). The production system was equipped with 300 W Yb-fiber laser operating in nitrogen atmosphere. Range of printing parameter values employed to produce the scaffolds are reported in Table 2.

To express in a single parameter the total energy conveyed by the laser beam to the sample unit volume, volumetric energy density E_v (VED), defined in equation (1) was considered (Gong et al., 2014, 2015):

$$E_v = \frac{P}{v\,h\,t} \tag{2}$$

P is laser power, v laser scanning speed, h hatching distance and t layer thickness. Volumetric energy density (E_v) used for producing the investigated graded scaffolds was 48 J/mm^3.

2.3. Experimental fractional density

The experimental value of fractional density ρ_{EXP} (%) of scaffolds and its uncertainty $\Delta\rho_{EXP}$ (%) were calculated according to equation (3):

$$\rho_{EXP}(\%) = \frac{m_s}{\rho_m V_s} * 100$$
$$\Delta\rho_{EXP}(\%) = \frac{\Delta m_s}{m_s} * \rho_{EXP}(\%) \tag{3}$$

where m_s is the experimentally measured scaffold mass, Δm_s the experimental error of the scaffold mass, V_S the total scaffold volume (cm^3) and ρ_m the material density. Scaffold average mass from 5 measurements were $m_{DI} = 3.67 \pm 0.04$ g and $m_{DO} = 2.41 \pm 0.05$ g for DI and DO geometries, respectively. The value of material density was assumed to be the nominal value of the alloy: $\rho_{mat} = 7.9$ g/cm^3 (Röttger et al., 2020; Li et al., 2019).

Table 2
Range of printing parameter values for the LPBF system employed to produce 316L SS graded lattice scaffolds.

Parameter	Range
Laser power [W]	200–270
Scan speed [mm/s]	400–1000
Hatching distance [mm]	0.10–0.14
Thickness [mm]	0.02–0.06

2.4. Structural characterization

Raw powder and up skin surface of DI and DO graded lattice scaffolds were investigated by Tescan VEGA3 scanning electron microscope (SEM), equipped with EDAX Elements microanalysis (EDS). The inner structure of scaffolds was observed by SEM, after cutting by diamond blade at half height (about 5 mm below the up-skin surface) and polishing. The state of DI and DO scaffolds after mechanical compression tests was also investigated by SEM.

Chemical composition of raw powder and scaffolds was obtained by averaging EDS results from 5 different areas at same magnification (500 ×).

Structural information of raw powder and scaffolds was collected by X-ray diffraction (XRD) by using a Bruker D8 Advance diffractometer operating at V = 40 kV and I = 40 mA, with Cu-Kα radiation, in the angular range 2θ = 30°–90° with step size Δθ = 0.05° and acquisition time t = 5 s/step. Pattern analysis was performed by DIFFRAC. EVA (Bruker AXS) software by using the PDF2 database of the International Centre for Diffraction Data (ICDD). Rietveld refinement of XRD patterns was carried out by the MAUD (Material Analysis Using Diffraction, http://maud.radiophema.com/) software, after calibration of the instrumental broadening by reference Al_2O_3 powder. Crystallographic structure of α-Fe (ferrite) and γ-Fe (austenite) phases used in Rietveld refinement were obtained from the Crystallography Open Database (COD, http://www.crystallography.net/cod/).

Peak shape analysis was carried out by OriginPro (Version, 2022. OriginLab Corporation, Northampton, MA, USA) software on XRD patterns measured in the reduced angular range 2θ = 42–45° with step size Δθ = 0.005° and acquisition time t = 30 s/step. Average crystallite size was evaluated from most intese peaks of Fe phases in the reduced angular range by using the Scherrer formula according to equation (4):

$$L = \frac{K\,\lambda}{\beta\,cos\,\theta} \tag{4}$$

with λ = 0.154056 nm, wavelength of Cu-Kα radiation, β Full Width at Half Maximum (FWHM), θ Bragg angle (unit: rad) and K a dimensionless number of the order of unity known as the Scherrer constant, which is related to crystallite size (Cullity, 1956).

Experimental lattice parameter values of α-Fe (ferrite) and γ-Fe (austenite) phases were estimated from XRD patterns measured in the reduced range. Nominal values of lattice parameters were obtained from ICDD files n. 6–696 and n. 33–397 for α-Fe (ferrite) and γ-Fe (austenite), respectively.

2.5. XμCT analysis

X-ray micro-computed tomography (XμCT) analysis was carried out

by Zeiss Metrotom 1500 tomographic system. Projections were acquired at V = 199 kV and I = 130 μA with 11.2 μm pixel size. A 0.75 mm Cu filter was used to enhance X-ray beam energy transmission. Acquisition time for projection was 2 s and frame averaging was used to reduce random noise of XμCT projections. Best compromise between image quality and acquisition time was obtained by averaging 3 image frames. Total rotation angle was 360° with 0.18° rotation step. A number of 2050 projections were converted into stack of 1017 cross-sectional slices, by bilinear interpolation. Scaffold average morphometric parameters such as closed porosity (P_C) and specific surface were obtained by Bruker SkyScan CT-analyzer software.

2.6. Mechanical tests

Compression tests were performed on 5 samples ($10 \times 10 \times 10$ mm^3) for each graded geometry (DI and DO) by an INSTRON 5567 machine, with 30 kN load cell at 0.5 mm/min speed, according to ISO 13314:2011 (ISO 13314:2011, 2011). Test stopped at 40% displacement from scaffold initial height. Compression data were plotted as load/strain curves for DI and DO geometries. Nominal elastic modulus (E) was calculated using regression linear statistics in the load range 50–500 N of the stress/strain curves. Compressive strength at 20% of strain (σ_{20}) and ultimate compressive strength (σ_{UC}) were determined, as reported by Onal et al. (2018), normalizing the applied compression load with the initial cross-section area of each sample (100 mm^2 for both geometries).

2.7. Biological tests

Scaffolds were firstly autoclaved and then irradiated on top and bottom surfaces with UV light for 30 min. After sterilization, samples were conditioned overnight with Dulbecco Modified Eagle's Medium (H-DMEM, Corning Inc., D6429) with 10% FBS (Corning Inc., 35-079-CV) and 1% penicillin/streptomycin (Thermo Fisher Scientific, 15,140,122). The conditioning mediums derived from DI and DO samples were used to evaluate cytotoxicity while the 3D graded scaffolds were used to investigate cell viability and adhesion.

MG-63 human osteosarcoma cells (ATCC, CRL-1427) were used to perform the biological assessment. Cells were cultured in H-DMEM composed of 1% penicillin–streptomycin and 10% FBS, in a humidified incubator at 37 °C, 95% air and 5% CO_2. For passaging trypsin/EDTA (trypsin 0.05%– EDTA 0.02% in PBS, Sigma-Aldrich, USAT4174) was used. Culture medium was refreshed every 3 days. For cytotoxicity evaluation, cells were seeded at density of 2×10^4/well in 96 well plates. After 24h from seeding, medium was replaced with material conditioned medium or its 1:2 and 1:5 dilutions, fresh medium was used as control. MTT assay was performed at 24 and 72h after medium change. For viability and morphological tests on 3D scaffolds, 8×10^4 cells were seeded on each sample in 100 μl of medium and incubated at 37 °C and 5% CO_2 for 30 min to promote cell attachment. After incubation, scaffolds were covered with fresh medium and cultured in a controlled atmosphere. MG63 viability was assessed by MTT assay and cellular morphology was observed by SEM after 24 h and 7 d from seeding.

The metabolically active MG63 were assayed by MTT (3-dimethylthiazol-2,5-diiphenyltetrazolium bromide, Sigma–Aldrich, M5655) according to the manufacturer's instructions. Briefly, the MTT stock solution (5 mg/ml) was diluted 1:10 in a cell culture medium, composed of H-DMEM without phenol red, and incubated at 37 °C for 3 h. After incubation medium was removed and DMSO was added to each well to dissolve the purple formazan crystals. Then the absorbance was quantified by spectrophotometry (MultiskanGo, Thermo Scientific) monitoring the absorbance at 570 nm with reference wavelength at 650 nm.

For SEM analysis, cells seeded scaffolds were fixed in 2% glutaraldehyde (MERCK, 4239) in 0.1 M sodium cacodylate buffer (Sigma, C-0250). After fixation, samples were washed with 7% sucrose in 0.1M cacodylate buffer and post-fixated with 1% osmium tetroxide (Electron Microscopy Sciences, 12,310) in 0.1 M sodium cacodylate buffer. Complete dehydration was achieved in graded alcohol series (25%, 50%, 70%, 80%, 95% and 100%) and Critical Point Dry was performed with hexamethyldisilane (HMDS, Sigma Aldrich, 440,191). Afterwards, samples were gold-sputtered by the Edwards Sputter Coater B150S equipment and observed with Tescan Vega 3 SEM.

2.8. Statistical analysis

The results statistical significance was evaluated by GraphPad Prism Software (v. 9.1.1), using two-way ANOVA with repeated measurements. Then, Tukey's post hoc test was carried out to highlight the main factors determining data variability. Statistical significance was set at ****$p < 0.0001$; ***$p < 0.001$; **$p < 0.01$.

3. Results

3.1. Powder characterization

SEM micrograph of raw powder is shown in Fig. 2. Particles are roundish with size ranging from 5 to 60 μm. Small satellite particles partially melted on larger particles are also visible (Fig. 2).

Experimental chemical composition from EDS is compared to nominal composition from the manufacturer data sheet (LPV CARPENTER Technology) in Table 3. Within uncertainties, values of experimental chemical composition are close to the nominal one.

XRD pattern of raw powder is reported in Fig. 3. Peaks revealed presence of the γ-Fe (austenite) face-centered cubic (fcc) phase (ICDD file n. 33–397) and the α-Fe (ferrite) body-centered cubic (bcc) phase (ICDD n. 6–696).

Rietveld analysis performed by the MAUD software estimated the amount of α-Fe (ferrite) in about 3 (wt.%).

3.2. Scaffold characterization

SEM observations of scaffolds up skin surface and inner structure are shown in Fig. 4. After manufacturing, few powder particles remained partially melted on the skin-up surface of both DI (Fig. 4a) and DO (Fig. 4c) geometries. Inner architecture of the DI geometry (Fig. 4b)

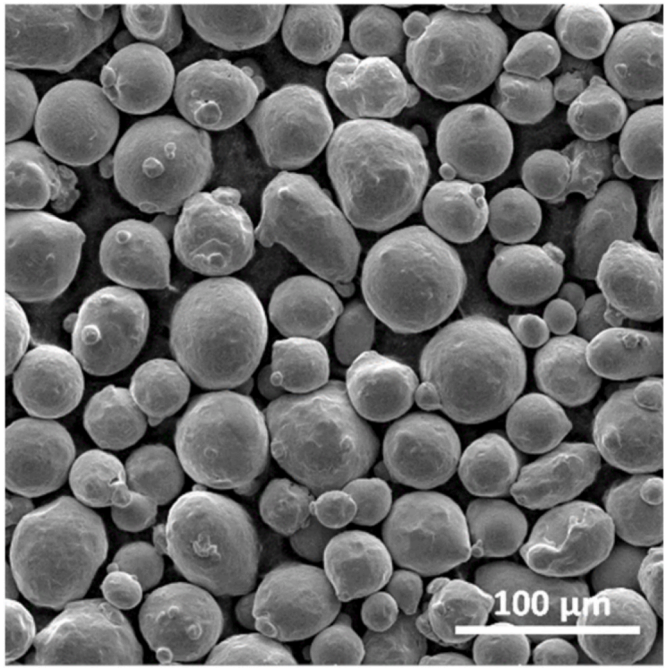

Fig. 2. SEM image of the 316L SS raw powder.

Table 3
Experimental chemical composition (wt.%) of 316L SS raw powder compared with nominal composition from the manufacturer data sheet (LPV CARPENTER Technology).

Element	Experimental composition (wt.%)	Nominal composition (wt.%)
C	–	≤0.030
Cr	17.67 ± 0.21	17.00 ÷ 18.00
Cu	–	≤0.75
Fe	bal.	bal.
Mn	1.6 ± 0.2	≤2.00
Mo	2.30 ± 0.03	2.00 ÷ 2.50
Ni	12.0 ± 0.3	12.00 ÷ 13.00
N	–	≤0.10
O	–	≤0.10
P	–	≤0.030
Si	0.74 ± 0.05	≤0.75
S	–	≤0.015

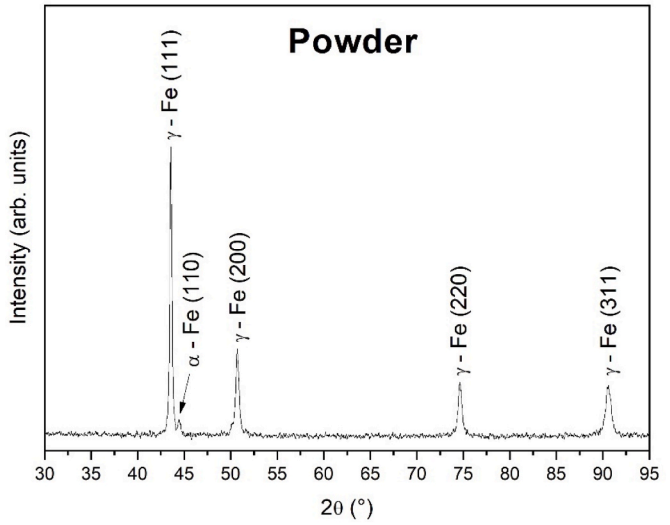

Fig. 3. XRD pattern of raw powder showing presence of γ-Fe (austenite) and α-Fe (ferrite).

shows quite unifom size of struts with some residual small pores due to the manufacturing process. On the contrary, the inner structure of the DO geometry (Fig. 4d) shows struts with low residual porosity and some discontinuity.

Pores are opened and interconnected in DO (Fig. 4d), but partially occluded with residual unmelted or partially melted powder in DI (Fig. 4b).

Experimental chemical composition of raw powder, DI and DO scaffolds is compared in Table 4. Scaffolds show a slight increase of Mn and Si as compared to powder, while amounts of Cr and Mo (ferrite stabilizers) as well as of Ni (austenite stabilizer) remain almost the same.

XRD patterns of DI and DO graded lattice scaffolds are reported in Fig. 5 along with XRD pattern of raw powder (PW), for comparison. In Fig. 5 all patterns are plotted in the angular range $2\theta = 35°–80°$ in square root intensity ($[\text{Intensity}]^{1/2}$) scale. Results clearly show presence of α-Fe (ferrite) in raw powder only, while scaffolds are entirely formed of γ-Fe (austenite), without any crystallographic fiber texture.

Peak shape analysis of patterns allowed obtaining exact peak angular position (2θ) and full width at half maximum (FWHM). For all samples, peak shape analysis was carried out on XRD patterns measured in the reduced angular range $2\theta = 42–45°$ with step size $\Delta\theta = 0.005°$ and acquisition time t = 30 s/step. In this reduced angular range also the presence of α-Fe (110) peak can be investigated. Results of peak shape analysis are reported in Table 5 as provided by OriginPro analysis software. Nominal lattice parameters for α-Fe ($a_{nom} = 0.28664$ nm) and

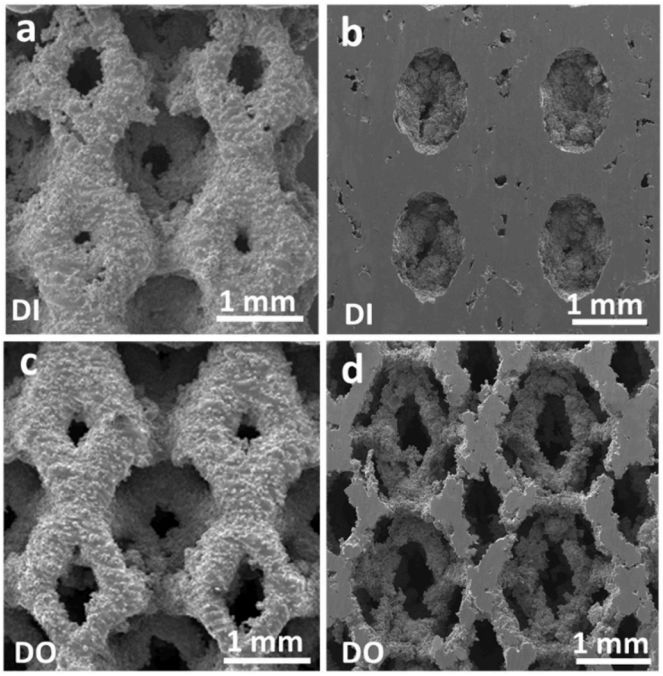

Fig. 4. SEM images of up skin surface (4a and 4c) and inner structure (4b and 4d) of DI and DO geometries.

Table 4
Experimental chemical composition (wt.%) of raw powder (PW), DI and DO graded lattice scaffolds.

Sample/ Element	Cr(wt. %)	Mn(wt. %)	Mo(wt. %)	Ni(wt. %)	Si(wt.%)	Fe
PW	17.7 ± 0.2	1.6 ± 0.2	2.30 ± 0.03	12.0 ± 0.3	0.74 ± 0.05	Bal.
DI	17.7 ± 0.2	2.5 ± 0.4	2.0 ± 0.2	12.1 ± 0.1	1.3 ± 0.4	
DO	18.0 ± 0.5	2.3 ± 0.5	2.1 ± 0.2	11.9 ± 0.2	1.5 ± 0.5	

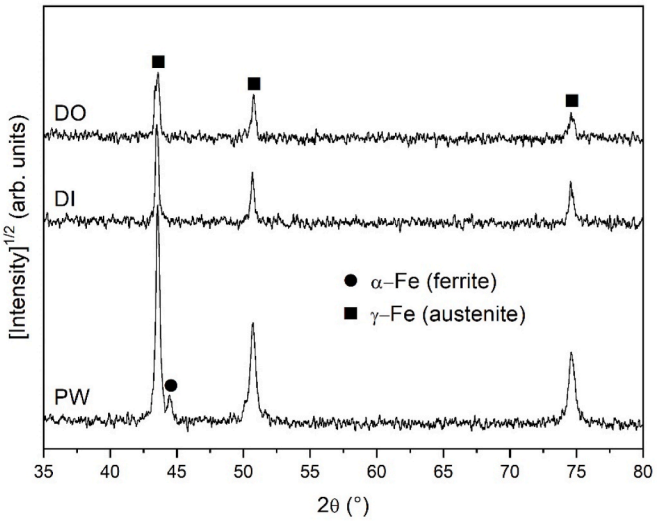

Fig. 5. XRD patterns of powder (PW), DI and DO graded lattice scaffolds plotted in square root intensity scale.

Table 5
Results of peak shape analysis performed in the reduced angular range 2θ = 42–45°. For all samples results are reported for γ-Fe (111) peak. For raw powder (PW) also results for α-Fe (110) peak are shown. 2θ (°) – peak angular position; FWHM (°) - Full width at half maximum; L – average size of crystallites from Scherrer equation; a_{exp} – experimental value of lattice parameter; $\Delta a/a_{nom}$ – relative difference (unit: %) between experimental and nominal lattice parameter ($\Delta a = a_{exp} - a_{nom}$).

Sample	Peak	2θ (°)	FWHM (°)	L (nm)	a_{exp} (nm)	$\Delta a/a_{nom}$ (%)
PW	γ-Fe (111)	43.5525 ± 0.0008	0.178 ± 0.002	47.5 ± 0.5	0.3596 ± 0.0001	0.14
	α-Fe (110)	43.672 ± 0.002	0.30 ± 0.03	28 ± 3	0.2929 ± 0.0002	2.18
DI	γ-Fe (111)	43.4715 ± 0.0008	0.116 ± 0.002	73 ± 1	0.3603 ± 0.0001	0.33
DO	γ-Fe (111)	43.487 ± 0.001	0.113 ± 0.003	75 ± 2	0.3601 ± 0.0001	0.28

γ-Fe (a_{nom} = 0.35911 nm) were obtained from ICDD file n. 6–696 and 33–397, respectively. Relative difference (unit: %) between experimental and nominal values of the lattice parameter is reported in the last column of Table 5 ($\Delta a/a_{nom} = (a_{exp} - a_{nom})/a_{nom}$).

In scaffolds, independently of geometry, γ-Fe (austenite) has lattice parameter very close to the nominal one ($\Delta a/a_{nom} < 0.4\%$), with almost same value of crystallites size (~74 nm). In powder, γ-Fe (austenite) is formed of smaller crystallites (~47 nm) with lattice parameter almost coincident to nominal value (Table 5), while α-Fe (ferrite) is formed of fine crystallites (size ~ 30 nm) with lattice parameter value about 2% higher than the nominal one.

XRD investigations carried out in the deformed region of scaffolds after compression did not evidence any deformation-induced phase transition.

The scaffold fractional density obtained from the STL file, the experimental measure and the XμCT analysis, as well as the specific surface from STL and XμCT are reported in Table 6 for DI and DO geometries.

3.3. Mechanical tests

Mechanical performances under compression of DI and DO graded lattice scaffolds are plotted in Fig. 6 as compressive load vs. compressive strain. As evidenced in Fig. 6, the mechanical behavior can be described by four regimes: I) Linear elastic regime; II) Plastic yielding regime; III) Plastic regime; IV) Densification.

Mechanical parameters of scaffolds reported as values of compressive strength at 20% strain (σ_{20}), ultimate compressive strength (σ_{UC}) and elastic modulus (E) are listed in Table 7 for DI and DO geometries.

SEM observations of scaffolds before and after mechanical compression tests are shown in Fig. 7.

Results clearly showed that plastic deformation of DI and DO graded lattice geometries firstly involved elementary cells with the smallest strut size (0.25 mm). This means that in the DI geometry plastic deformation followed by compaction of cells occurred in the most external layers on both sides of scaffold (Fig. 7a). On the contrary, in DO geometry deformation and compaction involved cells in the scaffold core with the thinnest struts (Fig. 7b).

Table 6
Fractional density of scaffolds obtained from the STL file, the experimental measurement (EXP) estimated from equation (3) and the XμCT analysis for DI and DO geometries. The specific surface of both geometries from the STL file and the XμCT analysis, are also reported for the investigated geometries (DI and DO).

Source	Fractional density (%)		Specific surface (mm^{-1})	
	DI	DO	DI	DO
STL	42	28	5	7
EXP[a]	46.5 ± 0.5	30.5 ± 0.6	–	–
XμCT	50	29	11	17

[a] Estimated from equation (3).

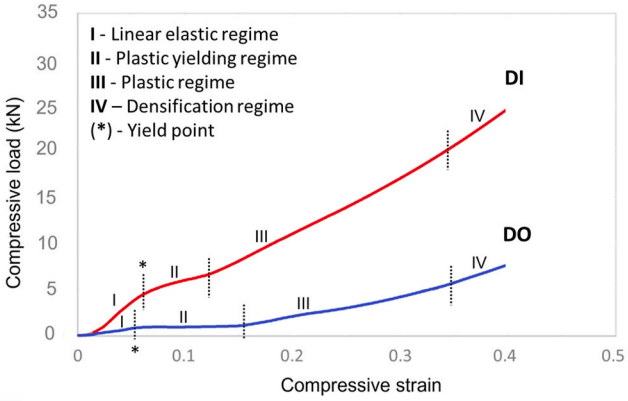

Fig. 6. Mechanical behavior under compression of DI (red curve) and DO (blue curve) graded lattice scaffold geometries. Four different mechanical regimes are indicated in the curves.

Table 7
Compressive strength at 20% strain (σ_{20}), ultimate compressive strength (σ_{UC}) and elastic modulus (E) for DI and DO graded lattice scaffolds. AV – average value; SD – standard deviation.

Geometry	σ_{20} [MPa]		σ_{UC} [MPa]		E [MPa]	
	AV	SD	AV	SD	AV	SD
DI	115	10	255	15	610	90
DO	23	3	80	6	310	100

3.4. Biological assessment of dense-in and dense-out structures

The indirect influence of medium derived from DI and DO scaffolds on cell viability was investigated by MTT test at 24 and 72 h after seeding. Fig. 8A shows the percentage of viable cells in comparison with control (ctrl). No significant differences were detected between cells incubated with not diluted or 1:2 diluted mediums derived from DI or DO scaffolds. Moreover, the viability of cells seeded on biomaterials and tissue culture plates (ctrl) was assessed by MTT assay after 24 h and 7 days from seeding (Fig. 8B). No significant differences between structures and ctrl were observed after 24h from seeding while on day 7, an exponential proliferation was assessed with a high degree of viability on 3D scaffolds in comparison with ctrl. Furthermore, significant differences were detected between structures, with the highest metabolically active cells on DO geometry.

SEM investigations revealed homogenous cell density across the entire scaffolds' surfaces. Cells spread on struts of both structures even after 24h of cultures (Fig. 8C and D) and, taking advantage of the surfaces' roughness, they accommodated their cell body in the inlets and concavities formed by partially fused particles and extended filipodia to the surrounding area. After 7 days of culture, cells covered both DI and DO scaffolds anchoring and spreading even on the semi fused particles and they also started to produce extracellular matrix (ECM), (Fig. 8E and F).

4. Discussion

Bone repair by scaffold needs a porous network allowing: 1) perfusion of fluid and gas, to assure nutrients and oxygen transport to the cells, thus enabling cell colonization, and 2) smooth distribution of stress at bone-implant boundary, to avoid bone resorption around the implant

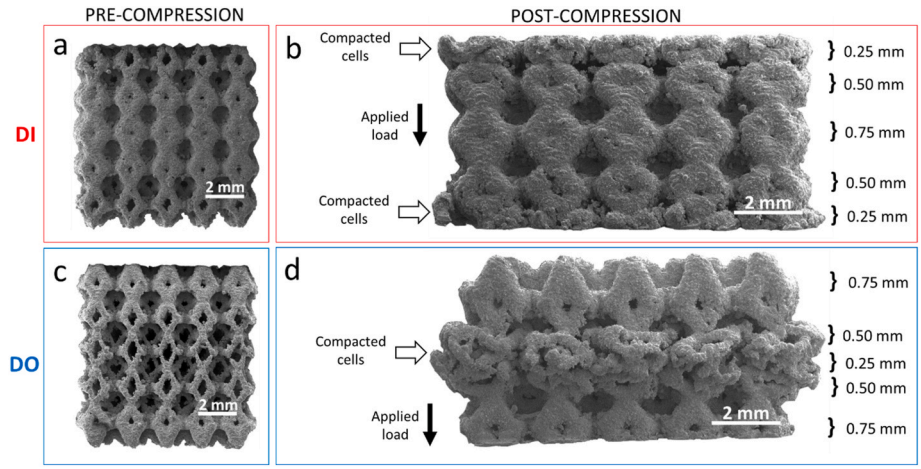

Fig. 7. SEM images of graded lattice scaffolds before and after compression test: a) and b) DI geometry, c) and d) DO geometry. Horizontal arrows evidence cell deformed to compaction. Vertical arrows show direction of applied load. Strut size of unit cell is reported on the right for each layer.

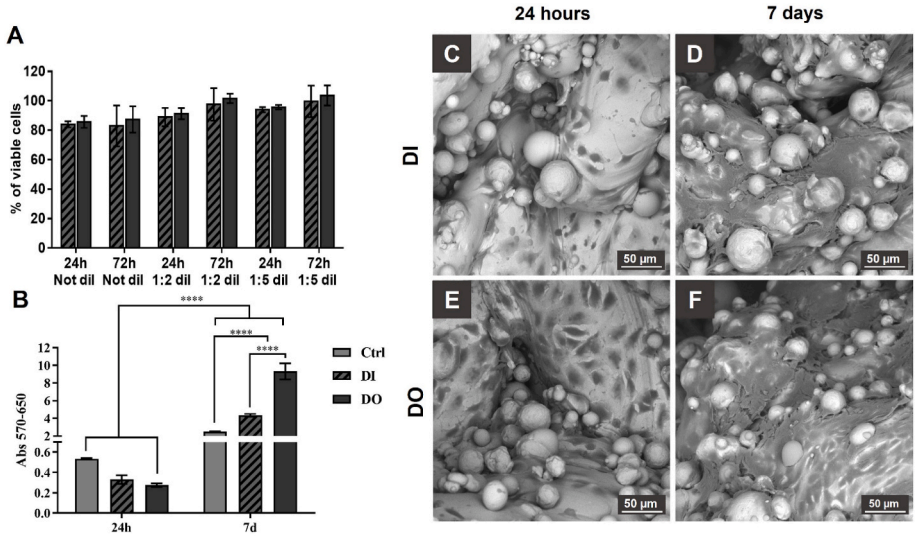

Fig. 8. Biological assessment of DI and DO graded lattice scaffolds. Histogram in A shows the viability of cells incubated for 24 h and 72 h with not diluted or diluted 1:2 and 1:5 conditioned medium derived from DI and DO scaffolds. Data are expressed as % over cells cultivated with normal medium. In Figure B the viability of cells seeded on DI and DO scaffolds was monitored after 24 h and 7 days; data are expressed as Absorbance. SEM panel (C–F) shows the MG63 morphology and adhesion on DI (C and D) and DO (E and F) scaffolds after 24 h (C and E) and 7 days (D and F) from seeding.

as a consequence of stress shielding phenomena (Al-Ketan et al., 2020). Graded lattice geometry obtained by spatially varying size of struts arranged in scaffold layers, satisfies both biomechanical requirements of bone tissue regeneration (Al-Ketan, 2021).

Starting from literature data reporting on regular lattice and optimized-lattice scaffolds in 316L stainless steel (316L SS), this study intends to demonstrate that graded geometry obtained by LPBF allows for designing scaffolds with improved biomechanical performances.

The driving idea of this study has been imported by similar work in the literature. In particular, this work is based on the method proposed by Li et al. (2016) that demonstrated how a graded cellular structure can provide mechanical properties superior to those previously reported for uniform structures, by appropriate design of the graded lattice. Li et al. (2016) applied the proposed method to a cellular structure based on the Ti6Al4V alloy with rhombic dodecahedral (RD) unit cell geometry. Onal et al. (2018) investigated the biomechanical behavior of Ti6Al4V continuous gradient structures produced by gradually changing the strut diameter of a body centered cubic (BCC) unit cell. This approach enables a smooth transition between unit cell layers and minimizes the effect of stress discontinuity within the scaffold. Recently, Caiazzo et al. (2022) reported on the mechanical properties of 17-4-PH stainless steel strut-based lattice structures in uniform and unidirectionally graded geometry, based on a BCC elementary unit cell.

In our previous works based on comparison of rhombic dodecahedral (RD) and diamond elementary unit cell geometries for uniform scaffold production we have found that RD geometry: a) in Ti6Al4V alloy-based scaffold facilitates removal of residual powder, and b) in PCL/HA composite scaffold provides a better 3D environment for cells adhesion and proliferation for scaffold colonization (Gatto et al., 2021a, 2021b). Therefore, starting from such results, two different graded lattice geometries based on the rhombic dodecahedral (RD) elementary unit cell (Fig. 1A) were considered in this experimental work. To obtain a graded lattice geometry the size of struts was gradually varied at each scaffold layer to avoid mismatch between contiguous layers, which was demonstrated to cause negative effects on mechanical properties and tissue ingrowth (Onal et al., 2018). In dense-in (DI) geometry strut size decreases in the build direction from core to edge, while in dense-out (DO) geometry strut size increases in the same direction (Fig. 1b and c). Both geometries were mirrored on the central horizontal axis, so that each scaffold was made up of five total layers (Fig. 1B and C).

It is worth to note that in this work we adopted the same unit cell geometry (RD) of Li et al. (2016), while the graded lattice was obtained by gradually changing the strut size as proposed by Onal et al. (2018). Furthermore, we adopted a unidirectional strut size variation as in the paper by Caiazzo et al. (2022). However, differently to the papers cited above (Onal et al., 2018; Li et al., 2016; Caiazzo et al., 2022) our

structures were mirrored through the central plane to obtain a symmetrical structure in the build direction, which is also the direction of the applied load in the compression tests.

The first step in successful production of improved scaffolds by LPBF was an optimization of printing parameters that were varied in the range reported in Table 2 to manufacture fully dense struts (Fig. 4C and D) (Irrinki et al., 2016; Slotwinski et al., 2014). Tolosa et al. (2010) were the first to demonstrate that relative density values higher than 99.9% could be achieved with laser power higher than 200 W. Kamath et al. (2014) suggested the use of volume energy density Ev to identify process parameters to produce components with relative density higher than 99%. Salarvand et al. (2022) investigated microstructure and corrosion resistance of fully dense samples of 316L SS produced by LPBF with $E_v = 100\ J/mm^3$.

Porosity is one of the most important parameters in scaffold production because it influences both mechanical and biological behavior. Porosity is generally distinguished in "closed porosity" (P_C) and "open porosity" (P_O). Micro-porosity inside the bulk material is responsible for P_C, which in turn determines material density, while macro pores linked to the elementary unit cell geometry constitute P_O. While P_O is determined by elementary unit cell design, P_C is influenced by printing parameters that control volume energy density E_v and cooling rate during the LPBF process.

Scaffold design was optimized to produce fully dense structures. Full density of our scaffolds was confirmed by the density value of the material calculated from the P_C value experimentally estimated from XμCT analysis. Therefore, from the P_C values obtained by XμCT the relative density, which is the ratio between the real and the nominal density ($\rho_{mat} = 7.9\ g/cm^3$) of the material, was estimated in 99.7% and 99.8% for DI and DO geometries, respectively.

It is worth noting that, in our case, the optimization of the deposition parameters (Table 2) allowed to produce fully dense scaffolds with a volumetric energy density value of 48 J/mm^2, which is about half the value (100 J/mm^2) reported by Salarvand et al. (2022) for the same material produced by the same LPBF technology, thus suggesting that full density of 316L SS can also be achieved using less energy in the LPBF manufacturing process.

Presence of residual powder in the core of DI structure (Fig. 4C) is mainly due to two combined effects, both linked to larger size of struts in the central layer (Fig. 1B): a) small size of open pores and b) high thermal capacity of core region. High thermal capacity reduces temperature decreasing rate in the scaffold core during cooling, which in turn induces partial melting of powder particles that remain attached to struts. The attached particles further reduce size of open pores, thus preventing the core unit cells from emptying of residual powder.

Microstructure of fully austenitic scaffolds in terms of chemical composition (Table 4), crystallite size and lattice parameter is the same for DI and DO geometries, within experimental uncertainties (Table 5). Furthermore, XRD investigation evidenced the absence of any fiber texture of γ-Fe (austenite) phase (Fig. 5). Usually, a strong crystallographic fiber texture with the <001> direction aligned along the build direction, which is the direction of fastest heat removal, is observed in the LPBF production of 316L SS parts (Bajaj et al., 2020). Texture can be explained by the fact that <001> direction is the fastest growing direction in cubic metal solidification, thus favoring growth of crystals with this crystallographic orientation aligned with temperature gradient (Gorsse et al., 2017). However, some authors have also demonstrated that in additive manufacturing fiber textures can be avoided by careful control of printing parameters (Suryawanshi et al., 2017; Wang et al., 2018). Texture control can also be used to avoid anisotropy in yield and tensile strength (Shamsujjoha et al., 2018). Therefore, similar microstructure and absence of texture in our samples suggest that the different mechanical behavior under compression of DI and DO scaffolds (Fig. 6) is fully due to different geometry of their elementary unit cell.

Onal et al. (2018) compared the mechanical response of the graded strut-based lattice structures to the uniform ones, showing that graded structures do not experience the expected sequential collapse of the scaffold layers, typical of the uniform structures. A layer-by-layer collapse of the structure is evidenced by oscillations in the stress-strain curve (Onal et al., 2018). F. Caiazzo et al. (2022) investigated the mechanical behavior of 17-4-PH stainless steel strut-based lattice structures in both graded and uniform conditions for three different values of fractional density, namely 15%, 25% and 35%. They reported oscillations in the stress-strain curve only for structures with 15% fractional density, independently on structure design (uniform or graded). Moreover, they also found that in the graded structures failure started from thinner struts, thus propagating to regions of higher density (thicker struts) (Caiazzo et al., 2022), while all uniform structures exhibited uniform collapse due to their regular geometry (Caiazzo et al., 2022).

As expected, the compressive curves of our graded scaffolds reported in Fig. 6 did not show any oscillation typical of uniform structures (Onal et al., 2018; Caiazzo et al., 2022). Furthermore, the fractional density of our scaffolds is about 50% and 30% for DI and DO geometries, respectively (Table 6). Such values of fractional density are well above 15%, which was the limit found by Caiazzo et al. (2022) for oscillations in the stress-strain curve of the 17-4-PH stainless steel strut-based lattice structures. The general shape of the compressive curves in Fig. 6 can be explained considering four regimes: I) elastic, II) plastic yielding, III) plastic and IV) densification. The range of strain values for each regime, as well as the range of load values involved, depend on scaffold geometry (Fig. 6). In the elastic regime (I in Fig. 6) compressive curves show linear behavior. At load values exceeding the elastic regime, the nominal yield point (asterisk in Fig. 6) is reached. At the yield point starts the plastic yielding regime (II in Fig. 6), where, as also observed by Caiazzo et al. (2022), the thinner struts (0.25 mm) of the scaffold start to collapse causing a yield plateau in the compressive curve. In the plastic regime (III in Fig. 6) complete collapse of elementary cells with lowest strut thickness occurs. After this, the collapsed material densifies giving rise to sharp increase of compression curve in densification regime (IV in Fig. 6). The final result of this deformation mechanism is shown in Fig. 7 for DI and DO geometries.

Therefore, the failure mechanism of graded lattice scaffolds based on the 316L SS is different from the mechanism active in uniform scaffolds (regular lattice or optimized lattice structure). In case of regular lattice or optimized lattice scaffolds based on the 316L SS, the compression curve presents oscillations due to the progressive collapse of layers that occur in plastic deformation regime (Zhong et al., 2019; Gatto et al., 2021a).

Results from the present work on mechanical behavior of DI and DO graded lattice geometries are compared in Table 8 to experimental results available in the literature for compression tests carried out on 316L SS regular lattice and optimized-lattice scaffolds. In Table 8 results from the following papers published in international journals were considered: Capek et al. (Čapek et al., 2016), Fusová et al. (Fousová et al., 2017), Xiao et al. (2018b), Cao et al. (2018), Zhong et al. (2019). It is worth to note that Zhong et al. (2019) reported only results obtained by finite element analysis (FEA) model developed for scaffolds under compression.

Due to strut orientation with respect to uniaxial compressive load, scaffold with tetrakaidekahedron unit cell (Zhong et al., 2019) and rhombic dodecahedron unit cell with hourglass-shaped struts (Cao et al., 2018), show localized 45° shear bands, during plastic yielding regime (Table 8). As deformation further increases beyond the plastic regime, localized deformation propagates to adjacent regions and densification of the entire structure occurs. Therefore, in tetrakaidekahedron unit cell (Zhong et al., 2019) as well as in rhombic dodecahedron unit cell with hourglass-shaped struts (Cao et al., 2018), failure of struts occurs on the basis of their orientation with respect to the applied load. From these results follows that regular lattices (Zhong et al., 2019; Čapek et al., 2016; Fousová et al., 2017; Xiao et al., 2018b) or optimized lattices with hourglass-shaped struts (Cao et al., 2018) do not allow to design the

Table 8
Comparison of scaffold failure mechanisms of our work with results experimentally obtained by Capek et al. (Čapek et al., 2016), Fusová et al. (Fousová et al., 2017), Xiao et al. (2018b) and Cao et al. (2018) and Zhong et al. (2019) who reported only on the finite element analysis (FEA) model developed for scaffolds under compression.

Reference	Lattice design	Failure mechanism
This work	Dense-In (DI) Dense-Out (DO)	Struts of smaller size initially involved in deformation. Time sequence of deformation depends on strut size. After compressive test, DI has outermost layers compacted, while DO shows an opposite behavior (Fig. 7 b and 7d)
Capek et al. (Ali and Sen, 2017) Fusová et al. (Al-Ketan et al., 2020)	Square-shaped pores 750 μm size separated by 250 μm thick struts. Total porosity 87%	Collapse of struts → complete collapse of cells → compaction of the porous structure
Xiao et al. (Li et al., 2016)	FCC unit cell scaffold size 18 × 18 × 18 mm^3. Total porosity 90%	No signs of local brittle failure. Lattice structure deformation is stable and smooth during the entire compression loading process
Zhong et al. (Wang et al., 2021)	Tetrakaidekahedron unit cell with cylindrical strut 1 mm diameter. Total porosity 60%. Scaffold size 25 × 25 × 25 mm^3. Ev = 90 J/mm^3	After stress plateau, densification occurs with struts completely collapsed. Due to the action of shearing and breaking at an angle of 45° to load direction, some struts fail, according to the finite element analysis (FEA) model
Cao et al. (Ren et al., 2022)	Rhombic dodecahedron unit cell with hourglass-shaped struts. Maximal section radius 0.71 mm, minimal section radius 0.42 mm. Relative density 0.12. Scaffold size 30 × 30 × 30 mm^3	Localized deformation is observed in intermediate areas of sample at 0.4 strain, causing 45° shear bands. As strain increases deformation propagates to adjacent regions, and then densification occurs. In the whole compression process any fracture or break of struts are absent.

compressive strategy of scaffold, because the progressive collapse of struts is followed by complete compaction of cells, accompanied by densification of the whole porous structure.

On the other hand, different deformation mechanisms are simultaneously active during compression of graded structures. Absence of oscillations in the compression curve (Fig. 6) and preferential compaction of layers with thinner struts (Fig. 7b and d) suggest that during deformation, thinner struts reach densification regime when thicker struts are still in plastic yielding regime. This means that time sequence of deformation in graded structures undergoes time shift depending on strut size. The predominant failure mechanism in graded structures initiates in correspondence of thinner struts, due to high stress concentrations on strut junctions, as reported by Onal et al. (2018) and Caiazzo et al. (2022).

Different distribution of strut size in graded geometries is the main factor influencing mechanical response. Consequently, DI geometry with lower thicker struts shows mechanical properties such as elastic modulus (E), ultimate compressive strength (σ_{UC}) and compressive strength at 20% strain (σ_{20}) always higher than DO (Table 7).

It is worth noting that σ_{UC} value for DO is very close to the experimental value of cortical bone (Gatto et al., 2021a).

From these results follows that careful control of strut size and layer sequence allows designing the mechanical response of graded scaffolds. However, mechanical behavior is also influenced by material microstructure including texture, both determined by printing parameters, that define cooling rate of melt pool during the layer-by-layer deposition. Therefore, complete design of mechanical response of graded structures goes through the combined control of printing parameters and lattice geometry.

In addition to mechanical characterization, biological validation was performed on DI and DO scaffolds to validate graded geometry in designing also appropriate biological performances (Čapek et al., 2016; Zuo et al., 2021). Furthermore, though 316L SS is widely used for orthopedic implants, LPBF process could affect scaffolds structural characteristics, by conditioning cell adhesion and viability.

Chemical composition of manufactured scaffolds in Table 4, shows an increased amount of Mn and Si in comparison to the feedstock powder, which instead was within the range of manufacturer specification (Table 3). This phenomenon is well-known, and Salman et al. concluded that the 316L SS samples produced by LPBF contain amorphous Mn–Si-rich spherical nano-precipitates (Salman et al., 2019). Therefore, indirect experiments were performed to evaluate the possible effects of the LPBF production process on MG-63 human osteosarcoma cells viability and to compare if geometries can stimulate different cell responses. Fig. 8A shows that scaffolds' conditioned mediums did not interfere with cell viability. Thus, the AM technique did not affect the already known properties of the material. Subsequently, direct interaction between cells and scaffolds was investigated. Cells exhibited spread morphology on struts already from 24 h of culture, also due to powder particles partially melted on the surface of scaffolds, which promote cell adhesion and increase anchoring surface points for pseudopodia and membranes (Fig. 8C and E). This strict interaction between cells and substrate observed by SEM (Fig. 8), is also shown by results of Onal et al. (2018), in which cells attach both on and between the unmelted powders, indicating that LPBF process is beneficial to cell attachment and further colonization. The assiduously pursued design strategy of coupling porous microarchitecture and rough surface finds reason in promoting scaffold integration and enhancing vascularization, cells-material interaction, and bone ingrowth (Fujibayashi et al., 2004; Wang et al., 2015; Cheng et al., 2017; García-Gareta et al., 2017; Ma et al., 2018). Moreover, 3D structures set the optimal requirements for fair colonization and increase in cellular activity (Keller et al., 1994) that was confirmed up to 7 days of culture. Cells actively proliferated and covered the struts of DI and DO scaffolds producing an abundant sheet-like elongated extracellular matrix, that mitigated the surface roughness (Fig. 8D and F).

Interestingly, DO geometry improved cell proliferation in comparison with DI (Fig. 8B). This promotion could be the effect of a better degree of diffusion of nutrients, as well as of the availability of oxygen for cells sustained by larger pores of DO scaffold core. This result seems apparently in contrast with findings by Onal et al. (2018) for the Ti6Al4V graded lattice scaffolds]. Onal et al. (2018) found that scaffolds with a thin strut diameter on the periphery (Dense-In) allowed cells to populate throughout the scaffold, whereas those with a thicker outer strut (Dense-Out) did not allow cells to migrate to the bottom surface, suggesting that cells were entrapped at the smaller pore size region (top surface). This mismatch could be imputable to the value of the specific surface, which in the paper by Onal et al. (2018) was the same for DI and DO structures, while in our work the specific surface value is higher for DO than for DI (Table 6). Specific surface, or surface to volume ratio, is a useful basic parameter for characterizing thickness and complexity of structures. The higher specific surface of DO with respect to DI geometry promotes a better cell attachment and growth, thus positively affecting the scaffold colonization.

5. Conclusions

Aiming to investigate the designing of scaffolds with improved biomechanical performances for bone tissue regeneration, two different

graded lattice structures based on 316L stainless steel (SS) were produced by laser powder bed fusion (LPBF). By varying layer-by-layer the strut size of the rhombic dodecahedral elementary unit cell in the build direction, dense-in (DI) and dense-out (DO) scaffolds were manufactured. The strut size decreased in DI and increased in DO from core to edge, with specular symmetry to the central layer. Structural, mechanical, and biological characterization was carried out, and the main results can be summarized as follows.

- raw powder with particle size in the range 5–60 μm and chemical composition compatible with the 316L SS was mainly formed of γ-Fe (austenite) with about 3 wt% α-Fe (ferrite);
- graded geometry scaffolds were manufactured by LPBF with combination of printing parameters that provided a volume energy density value $E_v = 48$ J/mm^3;
- independently of graded symmetry (DI or DO) scaffolds are fully dense ($\rho > 99.5\%$) and fully austenitic with crystallite size of about 75 nm, without any texture developed during the building process;
- compressive tests evidenced that plastic deformation in graded lattices firstly involves struts of smaller size. Therefore, time sequence of deformation undergoes time shift depending on strut size. Smaller struts reach densification when larger struts are still in plastic yielding regime, thus resulting in the different mechanical behavior of DI, and DO graded lattices. The DO graded geometry shows ultimate compressive strength value close to cortical bone;
- biological assessment at 24 h and 7 days incubation shows that DO graded geometry improves cell proliferation as compared to DI. This effect is mainly due to the larger pore size of DO that facilitates diffusion of nutrients and oxygen to cells.

In conclusion, principally due to biological and mechanical properties, graded lattice scaffolds of 316L SS can be considered for bone tissue regeneration. Improved biomechanical performances of scaffolds can be designed by properly controlling production parameters in the LPBF process and elementary unit cell geometry in graded structures.

CRediT authorship contribution statement

Maria Laura Gatto: Writing – original draft, Visualization, Investigation, Conceptualization. **Giorgia Cerqueni:** Writing – original draft, Validation, Investigation. **Riccardo Groppo:** Validation, Software, Methodology. **Eleonora Santecchia:** Writing – review & editing. **Emanuele Tognoli:** Investigation, Formal analysis. **Silvio Defanti:** Investigation, Formal analysis. **Monica Mattioli-Belmonte:** Writing – review & editing, Supervision, Resources. **Paolo Mengucci:** Writing – original draft, Supervision, Resources, Formal analysis, Conceptualization.

Declaration of competing interest

The authors declare that they have no known competing financial interests or personal relationships that could have appeared to influence the work reported in this paper.

Data availability

No data was used for the research described in the article.

Acknowledgements

This study was conducted under the collaboration with 3D4MEC S. r. l, Via Porrettana 48, 40037, Sasso Marconi (BO), Italy.

References

Al-Ketan, O., 2021. Programmed plastic deformation in mathematically-designed architected cellular materials. Metals 11 (10), 1622. https://doi.org/10.3390/met11101622.

Al-Ketan, O., Lee, D.W., Rowshan, R., Al-Rub, R.K.A., 2020. Functionally graded and multi-morphology sheet TPMS lattices: design, manufacturing, and mechanical properties. J. Mech. Behav. Biomed. Mater. 102, 103520 https://doi.org/10.1016/j.jmbbm.2019.103520.

Al-Mamun, N.S., Deen, K.M., Haider, W., Asselin, E., Shabib, I., 2020. Corrosion behavior and biocompatibility of additively manufactured 316L stainless steel in a physiological environment: the effect of citrate ions. Addit. Manuf. 34, 101237 https://doi.org/10.1016/j.addma.2020.101237.

Ali, D., Sen, S., 2017. Finite element analysis of mechanical behavior, permeability and fluid induced wall shear stress of high porosity scaffolds with gyroid and lattice-based architectures. J. Mech. Behav. Biomed. Mater. 75, 262–270. https://doi.org/10.1016/j.jmbbm.2017.07.035.

Bai, L., Gong, C., Chen, X., Sun, Y., Zhang, J., Cai, L., Zhu, S., Xie, S.Q., 2019. Additive manufacturing of customized metallic orthopedic implants: materials, structures, and surface modifications. Metals 9 (9), 1004. https://doi.org/10.3390/met9091004.

Bajaj, P., Hariharan, A., Kini, A., Kürnsteiner, P., Raabe, D., Jägle, E.A., 2020. Steels in additive manufacturing: a review of their microstructure and properties. Mater. Sci. Eng. 772, 138633.

Caiazzo, F., Alfieri, V., Campanelli, S.L., Errico, V., 2022. Additive manufacturing and mechanical testing of functionally-graded steel strut-based lattice structures. J. Manuf. Process. 83, 717–728. https://doi.org/10.1016/j.jmapro.2022.09.031.

Cao, X., Duan, S., Liang, J., Wen, W., Fang, D., 2018. Mechanical properties of an improved 3D-printed rhombic dodecahedron stainless steel lattice structure of variable cross section. Int. J. Mech. Sci. 145, 53–63. https://doi.org/10.1016/j.ijmecsci.2018.07.006.

Čapek, J., Machová, M., Fousová, M., Kubásek, J., Vojtěch, D., Fojt, J., Jablonskác, E., Lipov, J., Ruml, T., 2016. Highly porous, low elastic modulus 316L stainless steel scaffold prepared by selective laser melting. Mater. Sci. Eng. C 69, 631–639.

Cheng, A., Cohen, D.J., Kahn, A., Clohessy, R.M., Sahingur, K., Newton, J.B., Hyzy, S.L., Boyan, B.D., Schwartz, Z., 2017. Laser sintered porous Ti–6Al–4V implants stimulate vertical bone growth. Ann. Biomed. Eng. 45 (8), 2025–2035.

Cullity, B.D., 1956. Elements of X-Ray Diffraction. Addison-Wesley Publishing.

Dias, M.R., Fernandes, P.R., Guedes, J.M., Hollister, S.J., 2012. Permeability analysis of scaffolds for bone tissue engineering. J. Biomech. 45 (6), 938–944. https://doi.org/10.1016/j.jbiomech.2012.01.019.

du Plessis, A., Razavi, S.M.J., Benedetti, M., Murchio, S., Leary, M., Watson, M., Bhate, D., Berto, F., 2021. Properties and applications of additively manufactured metallic cellular materials: a review. Prog. Mater. Sci., 100918 https://doi.org/10.1016/j.pmatsci.2021.100918.

Fellah, M., Labaïz, M., Assala, O., Iost, A., Dekhil, L., 2013. Tribological behaviour of AISI 316L stainless steel for biomedical applications. Tribol. Mater. Surface Interfac. 7 (3), 135–149. https://doi.org/10.1179/1751584X13Y.0000000032.

Fousová, M., Kubásek, J., Vojtěch, D., Fojt, J., Čapek, J., 2017. 3D printed porous stainless steel for potential use in medicine. In: IOP Conference Series: Materials Science and Engineering, vol. 179. IOP Publishing, 012025. https://doi.org/10.1088/1757–899X/179/1/012025. No. 1.

Fujibayashi, S., Neo, M., Kim, H.M., Kokubo, T., Nakamura, T., 2004. Osteoinduction of porous bioactive titanium metal. Biomaterials 25 (3), 443–450.

García-Gareta, E., Hua, J., Orera, A., Kohli, N., Knowles, J.C., Blunn, G.W., 2017. Biomimetic surface functionalization of clinically relevant metals used as orthopaedic and dental implants. Biomed. Mater. 13 (1), 015008.

Gatto, M.L., Groppo, R., Bloise, N., Fassina, L., Visai, L., Galati, M., Iuliano, L., Mengucci, P., 2021a. Topological, mechanical and biological properties of Ti6Al4V scaffolds for bone tissue regeneration fabricated with reused powders via electron beam melting. Materials 14 (1), 224.

Gatto, M.L., Furlani, M., Giuliani, A., Bloise, N., Fassina, L., Visai, L., Mengucci, P., 2021b. Biomechanical performances of PCL/HA micro-and macro-porous lattice scaffolds fabricated via laser powder bed fusion for bone tissue engineering. Mater. Sci. Eng. C 128, 112300.

Gong, H., Rafi, K., Gu, H., Starr, T., Stucker, B., 2014. Analysis of defect generation in Ti–6Al–4V parts made using powder bed fusion additive manufacturing processes. Addit. Manuf. 1, 87–98. https://doi.org/10.1016/j.addma.2014.08.002.

Gong, H., Rafi, K., Gu, H., Ram, G.J., Starr, T., Stucker, B., 2015. Influence of defects on mechanical properties of Ti–6Al–4 V components produced by selective laser melting and electron beam melting. Mater. Des. 86, 545–554. https://doi.org/10.1016/j.matdes.2015.07.147.

Gorsse, S., Hutchinson, C., Gouné, M., Banerjee, R., 2017. Additive manufacturing of metals: a brief review of the characteristic microstructures and properties of steels, Ti-6Al-4V and high-entropy alloys. Sci. Technol. Adv. Mater. 18 (1), 584–610. https://doi.org/10.1080/14686996.2017.1361305.

Irrinki, H., Dexter, M., Barmore, B., Enneti, R., Pasebani, S., Badwe, S., Stitzel, J., Malhotra, R., Atre, S.V., 2016. Effects of powder attributes and laser powder bed fusion (L-PBF) process conditions on the densification and mechanical properties of 17-4 PH stainless steel. Jom 68 (3), 860–868. https://doi.org/10.1007/s11837-015-1770-4.

ISO 13314:2011, 2011. Mechanical Testing of Metals - Ductility Testing - Compression Test for Porous and Cellular Metals. International Organization for Standardization (ISO), Geneva, Switzerland.

Kamath, C., El-Dasher, B., Gallegos, G.F., King, W.E., Sisto, A., 2014. Density of additively-manufactured, 316L SS parts using laser powder-bed fusion at powers up

to 400 W. Int. J. Adv. Des. Manuf. Technol. 74 (1), 65–78. https://doi.org/10.1007/s00170-014-5954-9.
Keller, J.C., Stanford, C.M., Wightman, J.P., Draughn, R.A., Zaharias, R., 1994. Characterizations of titanium implant surfaces. III. J. Biomed. Mater. Res. 28 (8), 939–946.
Kong, D., Ni, X., Dong, C., Lei, X., Zhang, L., Man, C., Yao, J., Cheng, X., Li, X., 2018. Bio-functional and anti-corrosive 3D printing 316L stainless steel fabricated by selective laser melting. Mater. Des. 152, 88–101. https://doi.org/10.1016/j.matdes.2018.04.058.
Li, S., Zhao, S., Hou, W., Teng, C., Hao, Y., Li, Y., Yang, R., Misra, R.D.K., 2016. Functionally graded Ti-6Al-4V meshes with high strength and energy absorption. Adv. Eng. Mater. 18 (1), 34–38. https://doi.org/10.1002/adem.201500086.
Li, J., Chen, D., Zhang, Y., Yao, Y., Mo, Z., Wang, L., Fan, Y., 2019. Diagonal-symmetrical and midline-symmetrical unit cells with same porosity for bone implant: mechanical properties evaluation. JBE 16 (3), 468–479. https://doi.org/10.1007/s42235-019-0038-z.
Lodhi, M.J.K., Deen, K.M., Greenlee-Wacker, M.C., Haider, W., 2019. Additively manufactured 316L stainless steel with improved corrosion resistance and biological response for biomedical applications. Addit. Manuf. 27, 8–19.
Luo, J., Jia, X., Gu, R., Zhou, P., Huang, Y., Sun, J., Yan, M., 2018. 316L stainless steel manufactured by selective laser melting and its biocompatibility with or without hydroxyapatite coating. Metals 8 (7), 548.
Ma, L., Wang, X., Zhao, N., Zhu, Y., Qiu, Z., Li, Q., Zhou, Y., Lin, Z., Li, X., Zeng, X., Xia, H., Zhong, S., Zhang, Y., Wang, Y., Mao, C., 2018. Integrating 3D printing and biomimetic mineralization for personalized enhanced osteogenesis, angiogenesis, and osteointegration. ACS Appl. Mater. Interfaces 10 (49), 42146–42154.
Maconachie, T., Leary, M., Lozanovski, B., Zhang, X., Qian, M., Faruque, O., Brandt, M., 2019. SLM lattice structures: properties, performance, applications and challenges. Mater. Des. 183, 108137 https://doi.org/10.1016/j.matdes.2019.108137.
Majumdar, J.D., Kumar, A., Pityana, S., Manna, I., 2018. Laser surface melting of AISI 316L stainless steel for bio-implant application. Proc. Natl. Acad. Sci., India, Sect. A 88 (3), 387–403. https://doi.org/10.1007/s40010-018-0524-4.
Onal, E., Frith, J.E., Jurg, M., Wu, X., Molotnikov, A., 2018. Mechanical properties and in vitro behavior of additively manufactured and functionally graded Ti6Al4V porous scaffolds. Metals 8 (4), 200.
Peng, C., Izawa, T., Zhu, L., Kuroda, K., Okido, M., 2019. Tailoring surface hydrophilicity property for biomedical 316l and 304 stainless steels: a special perspective on studying osteoconductivity and biocompatibility. ACS Appl. Mater. Interfaces 11 (49), 45489–45497.
Ren, L., Wang, Z., Ren, L., Han, Z., Liu, Q., Song, Z., 2022. Graded biological materials and additive manufacturing technologies for producing bioinspired graded materials: an overview. Compos. B Eng., 110086 https://doi.org/10.1016/j.compositesb.2022.110086.
Röttger, A., Boes, J., Theisen, W., Thiele, M., Esen, C., Edelmann, A., Hellmann, R., 2020. Microstructure and mechanical properties of 316L austenitic stainless steel processed by different SLM devices. Int. J. Adv. Des. Manuf. Technol. 108 (3), 769–783. https://doi.org/10.1007/s00170-020-05371-1.
Salarvand, V., Sohrabpoor, H., Mohammadi, M.A., Nazari, M., Raghavendra, R., Mostafaei, A., Brabazon, D., 2022. Microstructure and corrosion evaluation of as-built and heat-treated 316L stainless steel manufactured by laser powder bed fusion. J. Mater. Res. Technol. 18, 4104–4113.
Salman, O.O., Gammer, C., Chaubey, A.K., Eckert, J., Scudino, S., 2019. Effect of heat treatment on microstructure and mechanical properties of 316L steel synthesized by selective laser melting. Mater. Sci. Eng. 748, 205–212.
Shamsujjoha, M., Agnew, S.R., Fitz-Gerald, J.M., Moore, W.R., Newman, T.A., 2018. High strength and ductility of additively manufactured 316L stainless steel explained. Metall. Mater. Trans. 49 (7), 3011–3027. https://doi.org/10.1007/s11661-018-4607-2.
Slotwinski, J.A., Garboczi, E.J., Stutzman, P.E., Ferraris, C.F., Watson, S.S., Peltz, M.A., 2014. Characterization of metal powders used for additive manufacturing. Journal of research of the National Institute of Standards and Technology 119, 460. https://doi.org/10.6028/jres.119.018.
Suryawanshi, J., Prashanth, K.G., Ramamurty, U., 2017. Mechanical behavior of selective laser melted 316L stainless steel. Mater. Sci. Eng. 696, 113–121. https://doi.org/10.1016/j.msea.2017.04.058.
Tolosa, I., Garciandía, F., Zubiri, F., Zapirain, F., Esnaola, A., 2010. Study of mechanical properties of AISI 316 stainless steel processed by "selective laser melting". following different manufacturing strategies. The International Journal of Advanced Manufacturing Technology 51 (5), 639–647. https://doi.org/10.1007/s00170-010-2631-5.
Wang, X., Schwartz, Z., Gittens, R.A., Cheng, A., Olivares-Navarrete, R., Chen, H., Boyan, B.D., 2015. Role of integrin α2β1 in mediating osteoblastic differentiation on three-dimensional titanium scaffolds with submicron-scale texture. J. Biomed. Mater. Res. 103 (6), 1907–1918.
Wang, X., Xu, S., Zhou, S., Xu, W., Leary, M., Choong, P., Qian, M., Brandt, M., Xie, Y.M., 2016. Topological design and additive manufacturing of porous metals for bone scaffolds and orthopaedic implants: a review. Biomaterials 83, 127–141. https://doi.org/10.1016/j.biomaterials.2016.01.012.
Wang, Y.M., Voisin, T., McKeown, J.T., Ye, J., Calta, N.P., Li, Z., Zeng, Z., Zhang, Y., Chen, W., Roehling, T.T., Ott, R.T., Santala, M.K., Depond, P.J., Matthews, M.J., Hamza, A.V., Zhu, T., Zhu, T., 2018. Additively manufactured hierarchical stainless steels with high strength and ductility. Nat. Mater. 17 (1), 63–71. https://doi.org/10.1038/NMAT5021.
Wang, Y., Huang, H., Jia, G., Zeng, H., Yuan, G., 2021. Fatigue and dynamic biodegradation behavior of additively manufactured Mg scaffolds. Acta Biomater. 135, 705–722. https://doi.org/10.1016/j.actbio.2021.08.040.
Xiao, Z., Yang, Y., Xiao, R., Bai, Y., Song, C., Wang, D., 2018a. Evaluation of topology-optimized lattice structures manufactured via selective laser melting. Mater. Des. 143, 27–37. https://doi.org/10.1016/j.matdes.2018.01.023.
Xiao, Z., Yang, Y., Xiao, R., Bai, Y., Song, C., Wang, D., 2018b. Evaluation of topology-optimized lattice structures manufactured via selective laser melting. Mater. Des. 143, 27–37.
Xu, S., Shen, J., Zhou, S., Huang, X., Xie, Y.M., 2016. Design of lattice structures with controlled anisotropy. Mater. Des. 93, 443–447. https://doi.org/10.1016/j.matdes.2016.01.007.
Zhong, T., He, K., Li, H., Yang, L., 2019. Mechanical properties of lightweight 316L stainless steel lattice structures fabricated by selective laser melting. Mater. Des. 181, 108076 https://doi.org/10.1016/j.matdes.2019.108076.
Zuo, W., Yu, L., Lin, J., Yang, Y., Fei, Q., 2021. Properties improvement of titanium alloys scaffolds in bone tissue engineering: a literature review. Ann. Transl. Med. 9 (15).